AGU PUBLICATIONS

JGR

Journal of Geophysical Research: Planets

RESEARCH ARTICLE
10.1002/2016JE005228

Key Points:
- The surface roughness of Mercury was measured at horizontal scales of 0.5 to 250 km
- In the smooth plains, the spatial density of tectonic landforms contributes to surface roughness at scales <20 km
- The enigmatic northern rise does not influence the observed roughness at scales of 0.5-250 km

Supporting Information:
- Supporting Information S1

Correspondence to:
H. C. M. Susorney,
hsusorn1@jhu.edu

Citation:
Susorney, H. C. M., O. S. Barnouin, C. M. Ernst, and P. K. Byrne (2017), The surface roughness of Mercury from the Mercury Laser Altimeter: Investigating the effects of volcanism, tectonism, and impact cratering, *J. Geophys. Res. Planets*, *122*, 1372–1390, doi:10.1002/2016JE005228.

Received 21 NOV 2016
Accepted 31 MAY 2017
Accepted article online 5 JUN 2017
Published online 29 JUN 2017

The surface roughness of Mercury from the Mercury Laser Altimeter: Investigating the effects of volcanism, tectonism, and impact cratering

H. C. M. Susorney[1], O. S. Barnouin[2,3], C. M. Ernst[2], and P. K. Byrne[4]

[1]Department of Earth and Planetary Sciences, The Johns Hopkins University, Baltimore, Maryland, USA, [2]The Johns Hopkins University Applied Physics Laboratory, Laurel, Maryland, USA, [3]Hopkins Extreme Material Institute, The Johns Hopkins University, Baltimore, Maryland, USA, [4]Department of Marine, Earth, and Atmospheric Sciences, North Carolina State University, Raleigh, North Carolina, USA

Abstract Surface roughness is a statistical measure of change in surface height over a given spatial horizontal scale after the effect of broad-scale slope has been removed and can be used to understand how geologic processes produce and modify a planet's topographic character at different scales. The statistical measure of surface roughness employed in this study of Mercury was the root-mean-square deviation and was calculated from 45 to 90°N at horizontal baselines of 0.5–250 km with detrended topographic data from individual Mercury Laser Altimeter tracks. As seen in previous studies, the surface roughness of Mercury has a bimodal spatial distribution, with the cratered terrain (dominated by the intercrater plains) possessing higher-surface roughness than the smooth plains. The measured surface roughness for both geologic units is controlled by a trade-off between impact craters generating higher-surface roughness values and flood-mode volcanism decreasing surface roughness. The topography of the two terrain types has self-affine-like behavior at baselines from 0.5 to 1.5 km; the smooth plains collectively have a Hurst exponent of 0.88 ± 0.01, whereas the cratered terrains have a Hurst exponent of 0.95 ± 0.01. Subtle variations in the surface roughness of the smooth plains can be attributed to differences in regional differences in the spatial density of tectonic landforms. The northern rise, a 1000 km wide region of elevated topography centered at 65°N, 40°E, is not distinguishable in surface roughness measurements over baselines of 0.5–250 km.

Plain Language Summary Surface roughness is a change in surface height over a given length scale after the effect of broad-scale slope has been removed and can be used to understand how geologic processes produce and modify a planet's topography at different scales. We used topography data from the Mercury Laser Altimeter to investigate Mercury's surface roughness. As seen in previous studies, the surface roughness of Mercury is either large or small depending where on the surface the surface roughness is measured, with the cratered terrain (dominated by the intercrater plains) possessing higher surface roughness than the smooth plains. The measured surface roughness for both geologic units is controlled by a tradeoff between impact craters generating higher surface roughness values and volcanism decreasing surface roughness. Subtle variations in the surface roughness of the smooth plains do not appear to be attributed to differences in age; instead, regional differences in the number of tectonic landforms likely influence roughness variations. The northern rise, a 1000 km wide region of elevated topography centered at 65°N, 40°E, is similar in surface roughness measurements to nearby regions over baselines of 0.5−250 km.

1. Introduction

The surface roughness of a planetary body is the assessment of changes in surface height over different horizontal length scales [*Shepard et al.*, 2001], after broad-scale slope effects have been removed. There have been many approaches to evaluate surface roughness, which have differing strength and weaknesses. Maps of surface roughness can be used to explore different geologic units [*Kreslavsky and Head*, 2000], to examine possible landing sites [*Anderson et al.*, 2003], and to investigate how geologic processes affect different scales of topography [*Shepard et al.*, 2001; *Morris et al.*, 2008; *Rosenburg et al.*, 2011]. The geologic interpretation of surface roughness is dependent on the horizontal scale at which the surface roughness is measured. Surface roughness at centimeter scales is sensitive to the regolith structure of the body, whereas at kilometer scales surface roughness is influenced by geologic landforms such as impact craters, volcanic

deposits, and tectonic structures. The type and resolution of the data employed in a roughness investigation determine the horizontal scale of surface roughness that can be assessed. The term "surface roughness" is commonly applied to the many different quantitative measures of roughness, including root-mean-square (RMS) deviation, RMS height, RMS slope, median differential slope, and the interquartile range of profile curvature. Readers are directed to *Shepard et al*. [2001] and *Kreslavsky et al*. [2013] for further detail on how to compute these measures and the sensitivity of each method.

The relationship between surface roughness and specific geologic processes has been investigated in previous studies of Earth, the Moon, and Mars [e.g., *Morris et al*., 2008; *Rosenburg et al*., 2011, 2015]. For example, *Yokota et al*. [2014] found a correlation with median differential slope (a measure of surface roughness) at a scale of 30 km and crater density for the Moon. At smaller scales on the asteroid 433 Eros, *Cheng et al*. [2002] found a correlation between regions of higher RMS deviation and the rim and exterior of large craters for scales of 5–300 m. Work has also been done to relate surface roughness at the scale of radar (i.e., centimeters) to specific geologic processes. For instance, *Morris et al*. [2008] studied the RMS deviation of Hawaiian volcanic flows and found that different volcanic features (e.g., ponded versus jumbled pahoehoe) have distinct roughness signatures.

Mercury is an interesting case study for investigating how specific geologic processes produce surface roughness at scales of hundreds of meters to kilometers. Mercury has only a few geologic processes acting to produce surface roughness at these scales and has no meaningful atmosphere (under which rates of erosion would increase). These major geologic processes include volcanism [e.g., *Strom et al*., 1975; *Spudis and Guest*, 1988; *Head et al*., 2008, 2011], tectonism [e.g., *Strom et al*., 1975; *Strom*, 1979; *Watters et al*., 2009; *Byrne et al*., 2014], and impact cratering [e.g., *Gault et al*., 1975; *Pike*, 1988; *Schultz*, 1988; *Strom et al*., 2008]. These processes have also operated widely on the Moon, which renders the satellite a useful analogue with which to understand surface roughness on Mercury.

One of the principal means by which the geologic units of Mercury can be categorized is on the basis of areal crater density. Specifically, the planet's smooth plains have relatively few impact craters compared with the intercrater plains [e.g., *Trask and Guest*, 1975; *Spudis and Guest*, 1988; *Denevi et al*., 2013; *Whitten et al*., 2014]. The intercrater plains include regions previously called heavily cratered terrain [e.g., *Trask and Guest*, 1975; *Strom et al*., 2008; *Whitten et al*., 2014]. Here we refer to all geologic terrain outside the smooth plains "cratered terrains," since it is dominated by the intercrater plains (but has not been all conclusively mapped as intercrater plains).

Several studies have investigated the surface roughness of Mercury. Before the MErcury Surface, Space ENvironment, GEochemistry, and Ranging (MESSENGER) mission, measurements of Mercury's topography were limited. Efforts to investigate Mercury's surface roughness used radar observations from the Arecibo observatory [*Harmon*, 1997, 2007; *Harmon et al*., 2007]. These studies focused on centimeter-scale roughness and identified regions of higher-surface and lower surface roughness values around different complex craters on Mercury. *Kreslavsky et al*. [2008] employed Earth-based radar topographic tracks of Mercury (34 tracks) to investigate surface roughness over longer horizontal baselines (40–250 km, the horizontal-scale surface roughness is measured over). They used the interquartile range of profile curvature for computing surface roughness, to make comparisons between Mercury, Mars, and the Moon. The study found that surface roughness values of the cratered highlands on the Moon are greater than the surface roughness on Mercury.

MESSENGER's Mercury Laser Altimeter (MLA) has provided topographic information that can be used to perform more detailed studies of the surface roughness of Mercury. *Talpe et al*. [2012] utilized the median differential slope to assess the surface roughness of impact craters that host radar-bright deposits [*Harmon et al*., 2001; *Chabot et al*., 2013]. Their results showed no difference between the surface roughness of craters that host radar-bright deposits and those that do not, across a wide range of horizontal baselines (0.8–5.6 km) [*Talpe et al*., 2012]. *Pommerol et al*. [2012] used a subset of the MLA data and the same measure of surface roughness (i.e., median differential slope) over a broader range of horizontal baselines (0.4–100 km) to compare the younger volcanic terrains on Mercury, Mars, and the Moon with each body's more heavily cratered terrain. This study found that Mercury's older cratered terrain is rougher than Mercury's younger terrain (i.e., the smooth plains) and that both Mercurian units have greater roughness values relative to the lunar mare and the Martian terrains (southern highlands and northern lowlands) but lower surface roughness values relative to the lunar highlands [*Pommerol et al*., 2012]. Using all the MLA data available at the time

(comprising less than a third of the total data that has ultimately become available), two studies [*Zuber et al*., 2012; *Yang et al*., 2013] mapped the median differential slopes on Mercury from 0°N to 90°N and 50°N to 90°N, respectively, with baselines of 0.8 to 12.6 km. Both studies noted the increased values of surface roughness of Mercury's cratered terrain relative to its smooth plains units. *Kreslavsky et al*. [2014] mapped the interquartile range of profile curvature at baselines of 0.7 to 11 km from 65°N to 84°N, and in addition to affirming the difference in surface roughness between the smooth plains and cratered terrains identified in previous studies, found that the northern rise (1000 km wide region of elevated topography centered at 65°N, 40°E) has surface roughness values indistinguishable from those of the surrounding smooth plains. These authors also proposed that their roughness measurements indicated a thicker regolith on Mercury relative to the Moon and that the lower surface roughness values of the interiors of flooded basins (e.g., Goethe) relative to surrounding volcanic terrains indicate a younger age for those interior deposits.

Recently, *Fa et al*. [2016] mapped RMS height, bidirectional slope, median differential slope, and the Hurst exponent from MLA data for horizontal baselines ranging from 0.39 to 15 km. Their findings are yet again consistent with the finding that the cratered terrains on Mercury have greater surface roughness values than do the smooth plains for RMS height, median absolute, and differential slope measurements. They attribute this difference to variations in areal crater density, as did previous studies [*Pommerol et al*., 2012; *Zuber et al*., 2012; *Yang et al*., 2013; *Kreslavsky et al*., 2014]. This is consistent with the observed morphology that the smooth plains have a smoother texture than the high crater density cratered terrain.

In this study, we use the entire MLA data set collected by the MESSENGER spacecraft to compute the surface roughness of Mercury over a much broader range of horizontal baselines, from 0.5 km to 250 km, than previous efforts. This work allows not only for a complete independent reassessment of the results of previous studies [*Kreslavsky et al*., 2014; *Fa et al*., 2016] but also reevaluation of previous findings with particular attention to how each of Mercury's three different geologic processes affect surface roughness. We have calculated surface roughness using a different measure of surface roughness (i.e., RMS deviation) than *Kreslavsky et al*. [2014], which is more sensitive to larger changes in topography. Our study also rigorously accounts for limitations in the MLA data set that include widespread changes in spacing between individual MLA points along MLA tracks, as well as poor geographical distribution of MLA tracks in some regions of the northern hemisphere of Mercury.

We document a new method to filtering MLA data for surface roughness calculations and we assess any biases in our filtering approach to enhance the robustness of the surface roughness results obtained. We have considered the effects of different spacing between individual MLA returns along a single track to determine surface roughness, in contrast to earlier work [e.g., *Fa et al*., 2016] (see section 2.1). Using a different measure of surface roughness and filtering technique highlights different aspects of the surface and reveal additional information about Mercury. We focus on using surface roughness to understand how the three major geologic processes on Mercury—impact cratering, volcanism, and tectonic deformation—produce and modify topography. We generate surface roughness maps from 45°N to 90°N (see Figure 1 for image and topography of the mapped region). The maps are compared with Mercury Dual Imaging System (MDIS) basemaps and MLA topography to examine how the three major geologic processes on Mercury—impact cratering, volcanism, and tectonic deformation—produce and modify surface roughness.

2. Methods

The high-resolution topographic data of Mercury returned by MLA permit the surface roughness of Mercury's northern region to be calculated, mapped, and analyzed. In this section, we discuss the advantages of and caveats to using MLA data, how we filtered the MLA data, how we calculated RMS deviation, and how these results were interpolated to produce regional surface roughness maps.

We use RMS deviation, the RMS of the difference in height over a specified baseline, as our measure of roughness for several reasons that are critical to our effort to understand how surface roughness and surface processes relate to one another. First, RMS deviation is widely used by the radar [e.g., *Shepard and Campbell*, 1999; *Shepard et al*., 2001], terrestrial landscape evolution [e.g., *Turcotte*, 1997; e.g., *Perron et al*., 2008], and the planetary science communities [e.g., *Kucinskas et al*., 1992; *Cheng et al*., 2002; *Rosenburg et al*., 2011], providing values of RMS deviation for other planets with which our results can be compared. Previous planetary science studies have shown that RMS deviation differs between various types of pahoehoe flow [*Morris et al*.,

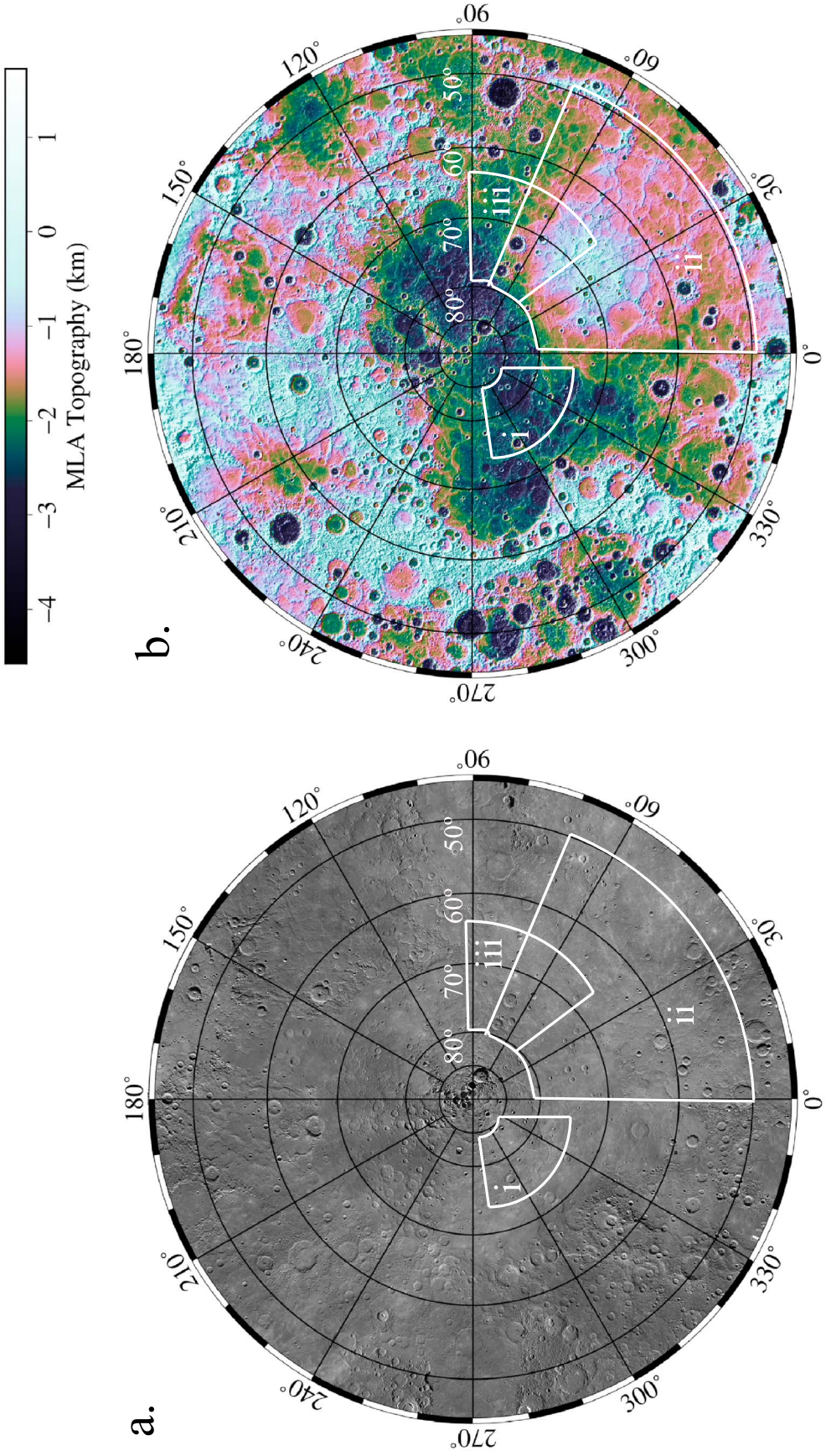

Figure 1. (a) Polar stereographic projection of a 43 pixel per degree MDIS basemap (at 750 nm) centered on 90°N and extending to 45°N. (b) MLA-interpolated topography of the same region. The boxes indicate several features that are discussed: (i) the 317 km diameter Goethe impact basin; (ii) the northern rise; and (iii) the 81 km diameter Gaudi crater and the 100 km diameter Stieglitz crater in the smooth plains.

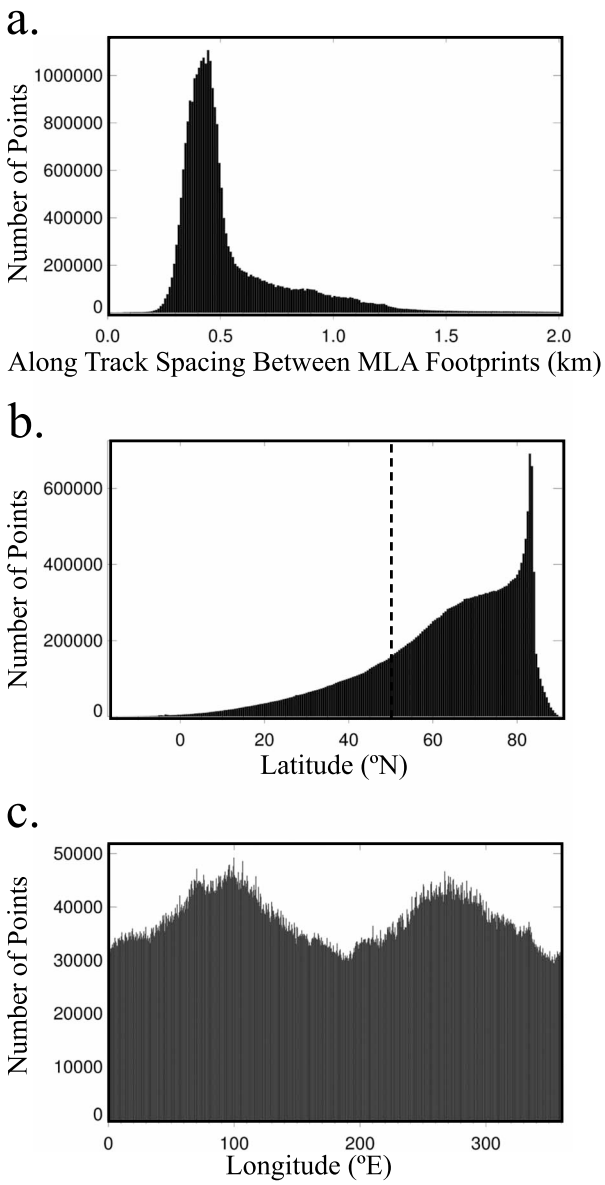

Figure 2. Histograms of topographic data. (a) The along track spacing between MLA points; the histogram was truncated at 2 km, but some MLA points are spaced greater than 2 km apart. (b) The latitude of MLA data; the dotted line denotes 45°N, where we truncated the maps in this study. (c) The longitude of the MLA data. The variation in MLA footprint spacing and latitude location limited the baselines over which the surface roughness could be measured.

2008], can be used to characterize landing sites on Mars [*Orosei*, 2003], can be used to assess the relative age of lunar geologic units [*Rosenburg et al.*, 2011], and can provide insight into the near-surface properties of asteroids such as 433 Eros [*Cheng et al.*, 2002]. Second, RMS deviation is frequently used to model topography of a surface as a self-affine fractal (a fractal that has different scaling in the x and y directions) if RMS deviation plotted against the baselines it was measured over in log-log space produces a linear plot, the exponent of the fit to the data is known as the Hurst exponent [*Turcotte*, 1997]. A single diagnostic Hurst exponent for a surface has been postulated to indicate that its topography is the result of a single geologic process that operates at many scales [e.g., *Shepard et al.*, 2001]. In contrast, a break in the slope of a plot of RMS deviation versus baseline (i.e., a change in Hurst exponent) may imply that more than one process is playing a role in influencing the observed topography, usually with one process influencing shorter baselines and another affecting topography at longer baselines. How Hurst exponents relate to geologic processes is better understood at small scales (i.e., radar studies) [*Morris et al.*, 2008]; at larger baselines (such as is the case for this study), the relationship of Hurst exponent to geologic processes is often unclear.

2.1. MLA Data

MLA tracks are concentrated in Mercury's northern hemisphere because of MESSENGER's highly elliptical orbit, which had an inclination around 82.5° and periapses in that hemisphere. MLA data have a ranging error of ~1 m [*Zuber et al.*, 2012]. The changing velocity of the spacecraft with respect to the surface resulted in uneven footprint spacing and distribution (Figure 2a). The latitudinal distribution of individual MLA points has a sharp peak at 82.5°N, corresponding to the initial orbital inclination (Figure 2b). We used data from all four MLA channels (channel 1 high, channel 1 low, channel 2, and channel 3). Data from channels 1 low, 2, and 3 were all filtered by the MLA team to remove spurious noise. We checked and found that using these noise-prone channels (channel 1 low, 2, and 3) did not introduce any additional uncertainties into our analysis. The use of the other channels is particularly important for increasing the total number of MLA returns available for analysis and for evaluating the surface roughness over very long baselines (since using all channels produced longer tracks). The study

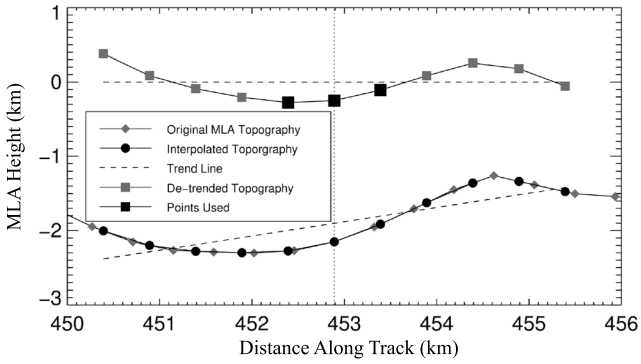

Figure 3. A schematic of how the spacing of MLA points is treated and the track detrended before calculation of Δh is performed (at L = 0.5 km). First, an MLA point of interest is selected (denoted by the vertical dotted line). Second, MLA points within 5 times the baseline of interest on either side of the point of interest ("Original MLA Topography") are interpolated to produce spacing equivalent to the baseline of interest ("Interpolated Topography"). Third, a linear trend line is fit to the interpolated data ("Trend Line") and used to remove broad-scale slopes, resulting in the De-trended Topography. Fourth, two Δh values are calculated for each point of interest using adjacent points ("Points Used") to either side.

therefore was able to investigate the roughness of Mercury with over 27,153,583 MLA returns (~6 million more than in *Fa et al*. [2016]).

We used individual MLA tracks to compute surface roughness for this study rather than gridded (i.e., interpolated) topographic surface model. Although the interpolation of MLA data to create gridded topographic surface models permits a higher number of surface roughness measurements (due to interpolation through areas where no MLA measurements are present), the gridding of MLA tracks masks the uneven footprint spacing and distribution, as well as any misalignment between tracks. The interpolated gridded product also smooths out topography, likely resulting in decreased surface roughness values [*Glaze et al*., 2003; *Barnouin-Jha et al*., 2005; *Robbins and Hynek*, 2013; *Susorney et al*., 2016]. Therefore, the use of individual MLA tracks permits a more accurate analysis of Mercury's surface roughness. Also, individual MLA tracks may have topographic mismatch with other tracks, which results in strips of topography (such as those shown in Figure 1b) sitting higher or lower than surrounding topography. By using solely individual MLA tracks this issue is not a problem, since surface roughness measured from tracks is relative to the track alone. A careful treatment of the uneven footprint spacing and distribution must be considered due to the relationship of surface roughness to the baseline over which it is measured.

2.2. Data Selection and Preparation

The main limiting factor in the calculation of surface roughness is the uneven spacing between adjacent MLA points (Figure 2a). An evaluation of this spacing is critical for calculating the surface roughness. Reliable surface roughness values are only calculated when MLA returns have horizontal spacing less than or equal to the baseline considered. Measurements of surface roughness from MLA tracks made without adjusting for uneven spacing would not produce a consistently reliable measurement of surface roughness at smaller baselines, in this case under about 5 km. The minimum baseline chosen was 0.5 km above the median spacing for most tracks. The maximum baseline was 250 km, limited by the length of the tracks (i.e., 4000–6000 km) and the need to detrend the track 10 times the length of the baseline of interest. The baselines used were 0.5, 0.6, 0.7, 0.8, 0.9, 1.0, 1.5, 2.0, 3.0, 4.0, 5.0, 6.0, 7.0, 8.0, 9.0, 10, 20, 30, 40, 50, 60, 70, 80, 90, 100, 125,150, 175, 200, and 250 km.

We developed a scheme, detailed in Figure 3, to select valid datapoints for our calculation of surface roughness. First, an MLA point was selected within an MLA track. Next, we checked that MLA points were available within a distance of 5 times the baseline of interest plus an additional 0.5 km on either side of the original MLA point to verify that the original point was not too near the end of that particular MLA track. The value of 5 times the baseline of interest was chosen so that the longer wavelength effects of slope could be removed over a distance 10 times the baseline of interest, based on the recommendations of *Shepard et al*. [2001]. Then we checked that the spacing between all points within 5 times the baseline of interest was less than that baseline. Depending on the baseline, 6–17 million MLA points met these criteria.

For MLA points where these criteria were satisfied, the MLA data within the 5 times baseline plus 0.5 km were used to derive a linearly interpolated topographic profile, wherein the topography was evenly sampled horizontally at a spacing equal to the baseline of interest. For this linear interpolation, the topographic height at the MLA point of interest was not modified. In the schematic we give in Figure 3, this

resulted in five points on either side of the point of interest that were 1 km apart. The interpolation process was compared with ~3000 MLA points where the adjacent points were not interpolated (with spacing similar to the baseline of interest). The interpolation method caused no statistically significant change in final RMS deviation measurements.

Next, the resulting topographic profile was linearly detrended to remove the effect of broader-scale slopes (e.g., the slopes of large impact craters). Finally, the change in height on either side of the MLA point in interest was measured, which gave two values of height (Δh) per MLA point that satisfied all of these criteria. This scheme was repeated at all baselines on all points in each MLA track analyzed.

For spatial analysis, the surface roughness of Mercury was gridded and mapped. The maps of surface roughness were truncated at 45°N due to a low spatial density of MLA tracks south of this latitude. The open-source software Generic Mapping Tools (GMT) was used for gridding and mapping [*Wessel et al.*, 2013].

For qualitative analysis, we produced maps where no consideration was made to the minimum value of n (the number of Δh used to calculate RMS deviation) required for a spatial bin used for gridding the surface. The gridding was designed to maximize the area mapped despite the low spatial density of MLA points below 70°N. In the supporting information, we compare maps of the 1 km baseline surface roughness with various spatial bin sizes, where larger bins have higher values of n (Figures S1 and S3). We demonstrate that although the qualitative regional RMS roughness variations on Mercury are not affected by the choice of n, the computed RMS deviation values are affected. This variation in RMS deviation (i.e., the stability of RMS deviation) is found to stabilize at $n \sim 100$ for Mercury (see Figure S4 in the supporting information). Therefore, we used the gridded maps for qualitative comparisons of roughness on Mercury and relied on the Hurst exponent and deviograms for quantitative comparisons (where we required $n > 100$).

During the gridding process, RMS deviation was calculated for spatial bins that scaled with 2 L (where L is the baseline), i.e., maps showing $L = 1$ km results were gridded with bins that were 2 km by 2 km. We chose to present interpolated maps here to ease in their interpretation. These gridded data sets were interpolated with continuous curvature splines (tension = 0.2: see *Smith and Wessel* [1990] for details). In the supporting information (Figures S1 and S2), we also show maps for $L = 1$ km with and without interpolation, to demonstrate that interpolation does not qualitatively affect the results. Detailed analysis of interpolated maps was made only after consulting noninterpolated maps to ensure that the spline fit did not introduce false local maxima or minima. For all baselines, the spatial distributions and values of surface roughness matched in both types of map.

2.3. RMS Deviation

RMS deviation (v) is calculated as the root-mean-square of the change of height (Δh) for a given baseline (L) [*Shepard et al.*, 2001]. It can be expressed as

$$v(L) = \left[\frac{1}{n}\sum_{i=1}^{n} \Delta h_i^2\right]^{\frac{1}{2}}, \quad (1)$$

where n is the total number of Δh values used in calculating $v(L)$ within a given spatial bin on the surface of Mercury.

2.4. Deviograms and Hurst Exponent

The calculation of deviograms (i.e., log-log plots of RMS deviation versus baseline) and Hurst exponents was performed separately from the gridding of maps (to ensure that $n > 100$). Deviograms provide a quantitative way to compare RMS deviations at different baselines between different regions of the planet and between Mercury and other worlds. The Hurst exponent can be calculated from the RMS deviation with the relation

$$v(L) = v_0 L^H, \quad (2)$$

where H is the Hurst exponent and v_0 is RMS deviation at the unit scale. The Hurst exponent is traditionally only calculated when the deviogram is linear in a log-log plot, implying that the surface has self-affine-like behavior. At larger scales, many planetary surfaces deviate away from self-affine behavior (e.g., the Moon) [*Rosenburg et al.*, 2011], and some surfaces show no self-affine-like behavior (e.g., the asteroid Itokawa)

[*Barnouin-Jha et al*., 2008] over the baselines measured. If a Hurst exponent can be fit to the deviogram, it may indicate that a single geologic process controls the surface roughness [*Shepard et al*., 2001].

We calculated deviograms and Hurst exponents for two principal Mercury terrain types: smooth plains [after *Denevi et al*., 2013] and cratered terrain (the region outside the smooth plains boundary: see section 1). Deviograms were calculated for MLA points where Δh could be calculated at all baselines (i.e., 500 m to 250 km). This constraint was placed to avoid the variability in the number of Δh measurements at smaller baselines across different regions, which would introduce biases into the deviograms. Both terrain types had more than 100 Δh values at all baselines.

3. Results

Maps of RMS deviation at baselines from 0.5 km to 250 km were produced from 45°N to 90°N. We divided the maps into three groups based on the baseline. The "small-scale" group contains maps with L ranging from 0.5 km to 2 km, the "medium-scale" group contains maps with L ranging from 2.5 km to 30 km, and the "large-scale" group contains maps with L between 40 and 250 km. The baseline groups do not demarcate abrupt changes in surface roughness distribution, but we chose this grouping to best illustrate our spatial observations for all maps.

3.1. Small-Scale Surface Roughness

At small baselines, i.e., L = 0.5–2 km (Figure 4), the surface roughness maps are dominated by a textural dichotomy between the smooth plains and the cratered terrain. Tectonic shortening structures (often termed "wrinkle ridges" and "lobate scarps") increase the surface roughness at L = 1 to 5 km but are a minor contributor to increasing surface roughness when compared with impact craters at this baseline. The major source of increased surface roughness within the smooth plains is large (i.e., >50 km diameter) complex impact craters and their surrounding ejecta deposits and associated secondary craters. The surface roughness of the cratered terrain is higher than the smooth plains, which matches morphological observations [e.g., *Strom et al*., 1975; *Denevi et al*., 2013], but the interiors of large impact craters in the cratered terrain have similar values as the smooth plains. For L = 0.5 km (Figure 4a), the regions around large complex craters in the smooth plains also have increased surface roughness values, but the differences in roughness relative to the surrounding smooth plains are not of the same magnitude as the L = 1 km map (Figure 4b). The northern rise—an enigmatic region of elevated topography at high northern latitudes some 1000 km across and about 1.5 km high, centered at 65°N, 40°E [e.g., *Zuber et al*., 2012]—is not discernible in the small-scale roughness maps.

3.2. Medium-Scale Surface Roughness

Results for surface roughness for medium baselines, i.e., L = 2.5–30 km (Figure 5), show the same overall trends as the small-scale baselines: a bimodal distribution in surface roughness between the smooth plains and cratered terrain. The role of impact craters in influencing surface roughness is about the same for these baselines as for smaller baselines (i.e., $L \leq 2.0$ km), with impact craters increasing their proximal surface roughness (again, because of their ejecta deposits and secondary crater fields). For L = 5 km (Figure 5a); the smooth plains once more have resolvably lower surface roughness than the cratered terrain at these scales. At L = 20 km (Figure 5b), the regions around large complex craters do not have the same elevated surface roughness values as observed for $L \leq 5$ km, but surface roughness is increased within the crater itself. Small tectonic landforms, increase surface roughness at L = 5 km, but not at L = 20 km (Figure 5). As with smaller values of L (i.e., <2 km), maps in this intermediate range show no surface roughness evidence for the northern rise.

3.3. Large-Scale Surface Roughness

For large baselines, i.e., L = 40–250 km (Figure 6), the bimodal distribution of surface roughness between the smooth plains and the cratered terrain is still present, but the effect of individual craters on regional surface roughness diminishes as the baseline increases. The northern rise is still not visible at L = 80 km (Figure 6a), although possible evidence of increased surface roughness corresponding to this feature may be seen at L = 250 km (Figure 6b).

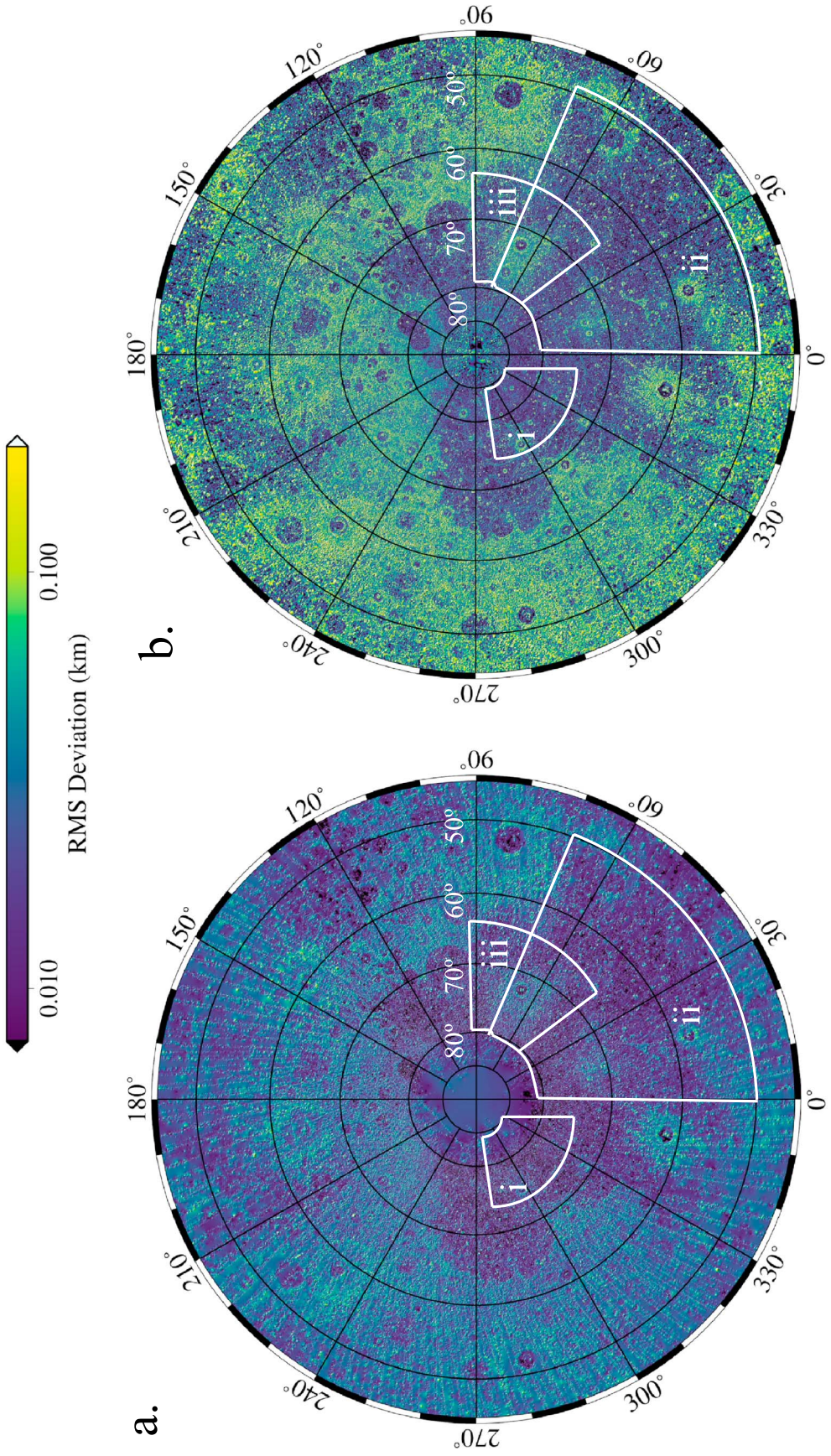

Figure 4. The surface roughness from 45°N to 90°N at the (a) 500 m baseline and (b) 1 km baseline. The white boxes match those defined in Figure 1. The region north of 85°N in Figure 4a has fewer measurements of surface roughness in that area because of missed MLA returns and relatively large spacing between the recorded data. In both Figures 4a and 4b there is a bimodal difference in the distribution of surface roughness values, with higher-surface roughness values in the intercrater plains compared to the smooth plains (see Figure 8). The northern rise (box ii) has the same values of surface roughness as the surrounding terrain at these baselines. The ejecta around large secondary craters have higher roughness values (box iii). The maps are in polar stereographic projection centered at 90°N.

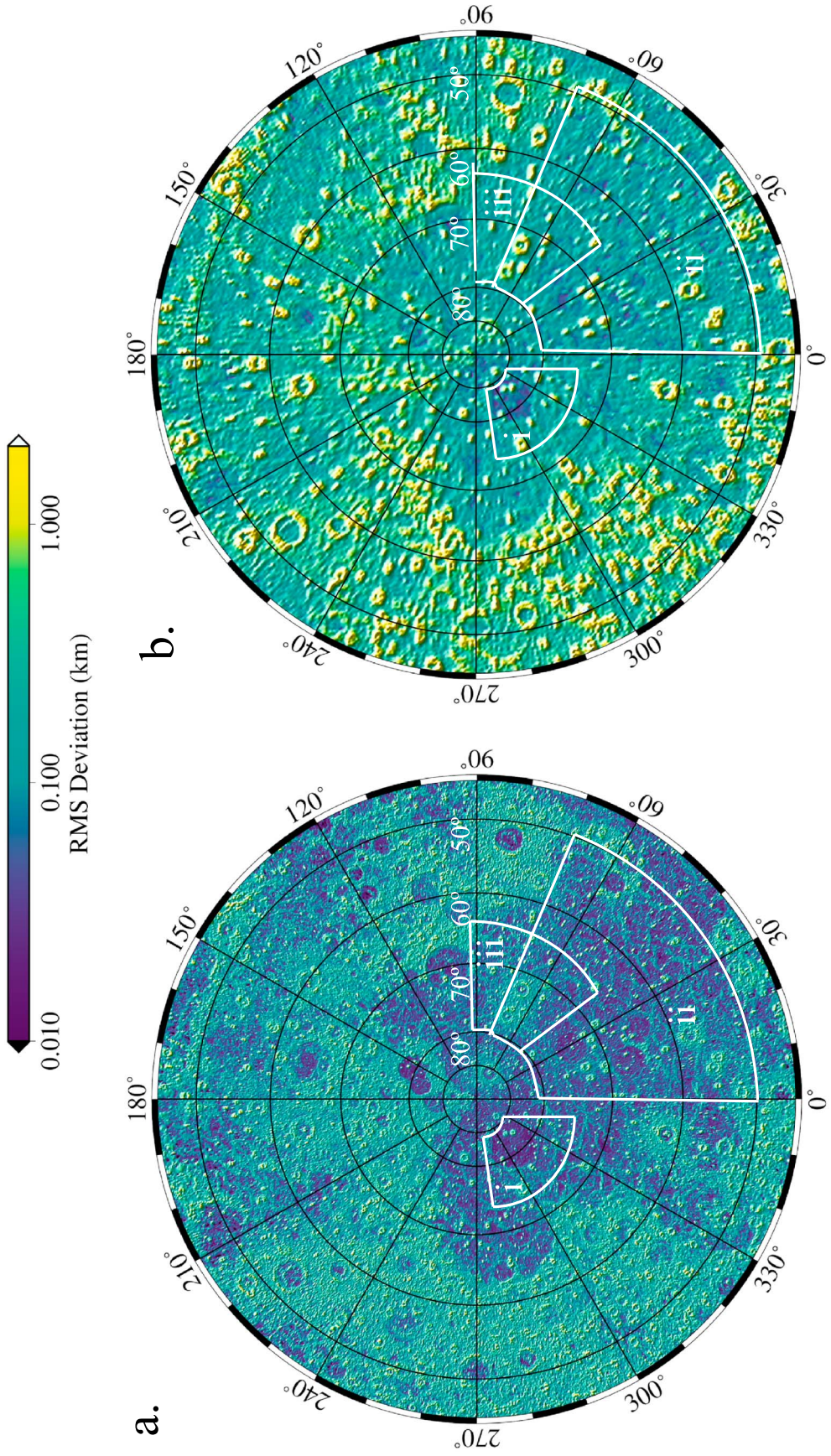

Figure 5. The surface roughness from 45°N to 90°N at the (a) 5 km baseline and (b) 20 km baseline. In Figure 5b the map has a less crisp appearance arising from the larger bin sizes used for the calculation of RMS deviation at this spatial scale. At these baselines, the general bimodal trend in surface roughness remains. In Figure 5a, the tectonic shortening structures in the smooth plains are particularly visible as smaller linear patterns of increased roughness (see the zoom in of i particularly the outside of Goethe Basin, Figure 9b). In Figure 5b, the elevated surface roughness at large craters is due to the crater cavity and not from surface textures exterior to the crater (which include the ejecta and secondary craters) as is the case for smaller baselines (box i). The maps are in polar stereographic projection centered at 90°N.

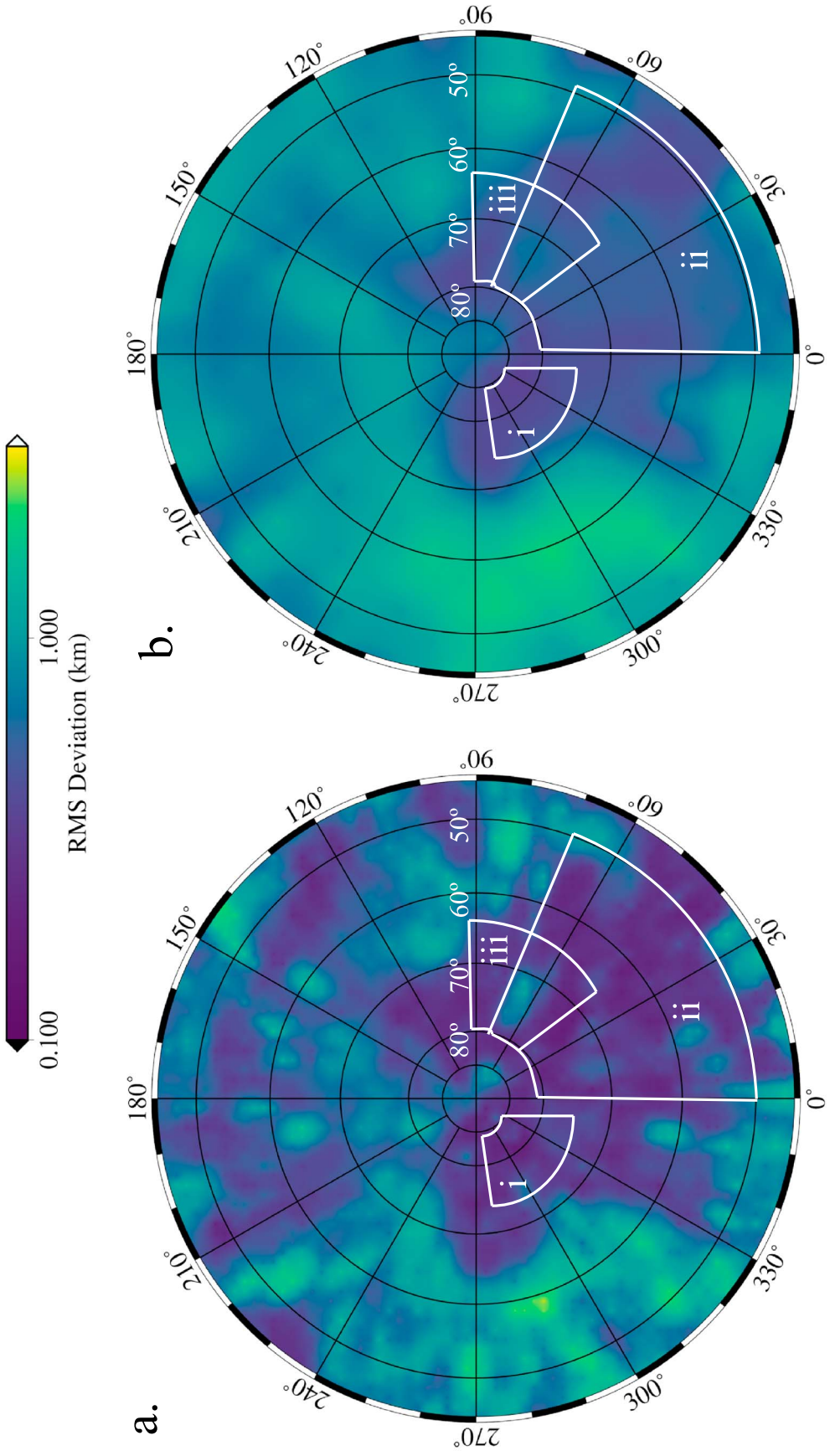

Figure 6. The surface roughness from 45°N to 90°N at the (a) 80 km baseline and (b) 250 km baseline. The bimodal trend in surface roughness between the two major surface units, apparent at smaller baselines, is again present in both Figures 6a and 6b. The effect of individual craters is more subdued at these longer baselines. The maps are in polar stereographic projection centered at 90°N.

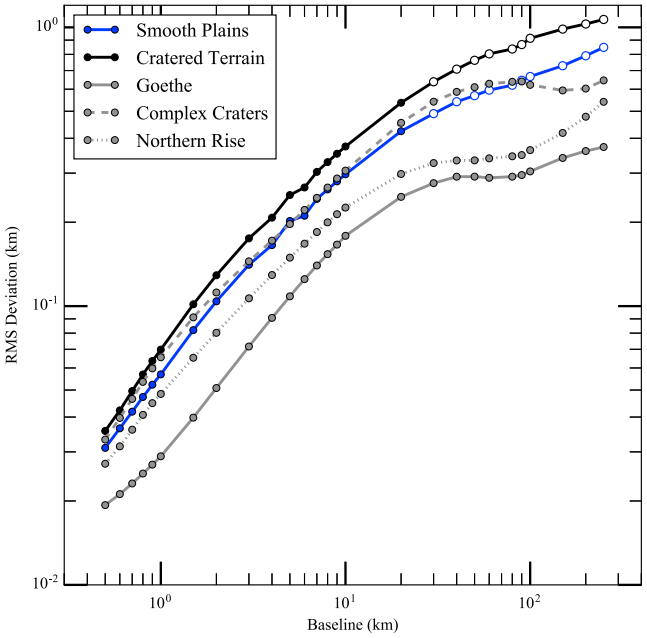

Figure 7. Deviogram of the smooth plains, cratered terrain, Goethe Basin interior, the northern rise, and the complex craters Gaudi and Stieglitz (including the craters' ejecta) from baselines of 500 m to 250 km. The Hurst exponent was fit at baselines from 0.5 to 1.5 km. Above 1.5 km, the deviogram begins to curve. The "dip" in the deviogram for Goethe and the northern rise at L = 30 km as compared to the whole smooth plains is due to the deviograms being calculated more than a baseline away from the smooth plains-cratered terrain border. The error in individual MLA measurements is ~1 m, which is not resolved on this graph.

3.4. Deviogram and Hurst Exponent

A deviogram of all smooth plains units, as defined by *Denevi et al.* [2013] (Figure 7), shows that consistent with morphological observations, this geologic unit possesses lower surface roughness values than the cratered terrain in our region of interest (Figure 8) for all baselines we consider here. The shape of the log-log deviogram is linear from 500 m to ~1.5 km and then begins to gradually curve, resulting in a lower slope. The turnover occurs at a smaller baseline than reported in *Fa et al.* [2016]. A linear log-log behavior of the deviogram implies a self-affine (possibly fractal) nature to the surface roughness, which may correspond to one dominant geologic process if that process produces topography that scales with size. Curvatures in a deviogram may indicate either the interplay of several processes that together influence the measured surface topography [*Shepard et al.*, 2001; *Rosenburg et al.*, 2011] and/or the presence of a geologic process that does not scale with size (i.e., flood volcanism). Hurst exponents were calculated from the deviogram over at baselines 0.5 km to 1.5 km; we found values of $H = 0.95 \pm 0.01$ for the cratered terrain and 0.88 ± 0.01 for the smooth plains (with a v_o of 0.07 km and 0.06 km, respectively).

The deviograms of the smooth plains and cratered terrain units are denoted as open circles after L = 30 km due to possible boundary effects at these baselines. Closer to the boundaries between terrain types, long-baseline RMS deviation calculations incorporate data from the other geologic unit, resulting in surface roughness values that are lower for the cratered terrain and higher for the smooth plains when compared to smaller, continuous regions of each unit lying far from the unit boundaries. In the smooth plains, in particular, away from the boundary, deviograms of the northern rise and a basin Goethe (Figure 7, both geographically centered away from the edge of the smooth plains) show a plateau of surface roughness values from L = 30–100 km, matching observations in the maps. The Hurst exponent results for the smooth plains and cratered terrain are not affected by the border of the units due to the small L over which they were calculated.

4. Discussion

In the following section, we investigate how different geologic processes might influence the measured surface roughness of Mercury. In particular, we consider volcanism, impact cratering, and tectonic deformation as mechanisms that affect the surface roughness at different scales. The Hurst exponent is used to provide quantitative comparisons with previous studies of surface roughness on Mercury and other bodies.

4.1. Volcanism

Volcanism is a dominant resurfacing agent for large parts of Mercury [*Strom et al.*, 1975; *Head et al.*, 2008; *Marchi et al.*, 2013; *Byrne et al.*, 2016]. On the basis of surface textures, spectral contrast with surrounding

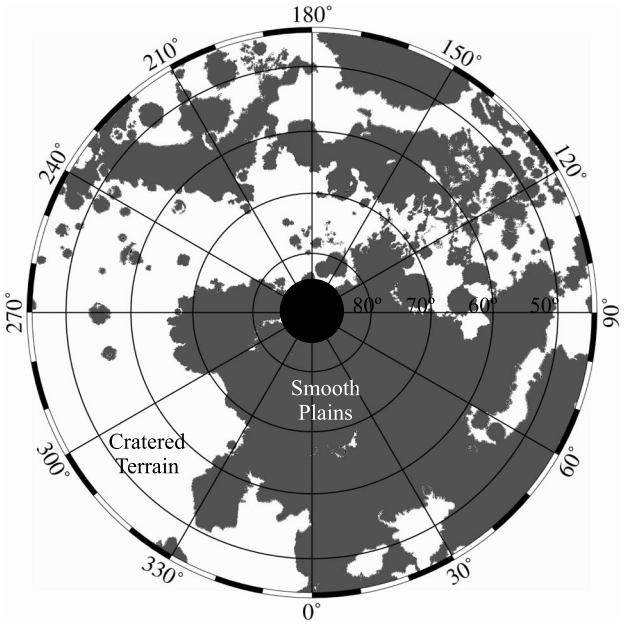

Figure 8. The smooth plains (shown in gray) from 45°N to 90°N mapped by *Denevi et al.* [2013]. In this paper, regions outside of the smooth plains are referred to as the cratered terrain. The map is in polar stereographic projection centered at 90°N. The black circle in the center represents the area not mapped by *Denevi et al.* [2013].

terrain, superposition relations, and infilling of preexisting topography [e.g., *Head et al.*, 2008; *Denevi et al.*, 2009, 2013], the vast northern smooth plains are thought to be volcanic in nature [*Head et al.*, 2011; *Ostrach et al.*, 2015]; this single smooth plains unit make up the majority of this type of plains assessed here. Because of the areal extent of the smooth plains, the areal homogeneity of superposed impact craters, and the lack of obvious source vents, the primary mode of emplacement for the northern smooth plains is likely flood-basalt-style volcanism [*Head et al.*, 2011], where basaltic lavas spread over large regions relatively quickly [*Ostrach et al.*, 2015]. Flood-basalt-style volcanism acts to "reset" the crater retention age of a surface [*Head et al.*, 2011; *Ostrach et al.*, 2015], which in turn reduces its surface roughness (the ejecta of large impact craters can also reset surface roughness, but this does not appear to influence the data here). Accordingly, we find here that roughness values at all baselines we considered are consistent with having been reduced by flood-basalt-style volcanism in Mercury's northern hemisphere. Variations in the surface roughness in the smooth plains are not due to rapid emplacement of basaltic lavas; instead, the variations can be traced to differences in areal density and relief of tectonic landforms and the presence of large complex craters that if locally modify the surface roughness.

4.2. Tectonics

Despite the effect of flood volcanism upon surface roughness, some variations in this property of the northern smooth plains exist; we attribute these variations to a combination of large impact craters (greater than 50 km in diameter) and tectonic landforms, most of which are interpreted to reflect crustal shortening on the basis of their positive relief. The vast majority of these landforms are the smooth-plains structures (commonly called "wrinkle ridges" and "lobate scarps") described by *Byrne et al.* [2014] as positive-relief tectonic landforms interpreted to represent a combination of thrust faulting and associated folding and manifest as sinuous arches and crenulations with variable sinuosity, breadth, and height. Such tectonic structures contribute to variations in (and increases to) surface roughness to a lesser extent than the more substantive effects of flood volcanism. The presence of tectonic shortening structures at smaller baselines (under 20 km) is still important enough that these structures must be considered when making comparative assessments within the smooth plains. While contractional features dominate Mercury's tectonic landforms, extensional features are present [e.g., *Strom*, 1979]; however, they do not modify the surface roughness at the baselines measured here.

4.2.1. Small Tectonic Features

A previous study of the surface roughness of Mercury proposed that the smooth plains unit within Goethe basin (Figure 1b box i), situated within the northern smooth plains, is younger than other regions of the northern smooth plains on the basis of its lower surface roughness values [*Kreslavsky et al.*, 2014]. The authors concluded that small craters were the main contributors to the relative increase of surface roughness outside of Goethe, and thus, Goethe is younger than the surrounding plains. Here too, we observe a similar decrease in surface roughness values within the basin (Figure 9b) at all baselines (see deviogram of Goethe in Figure 7).

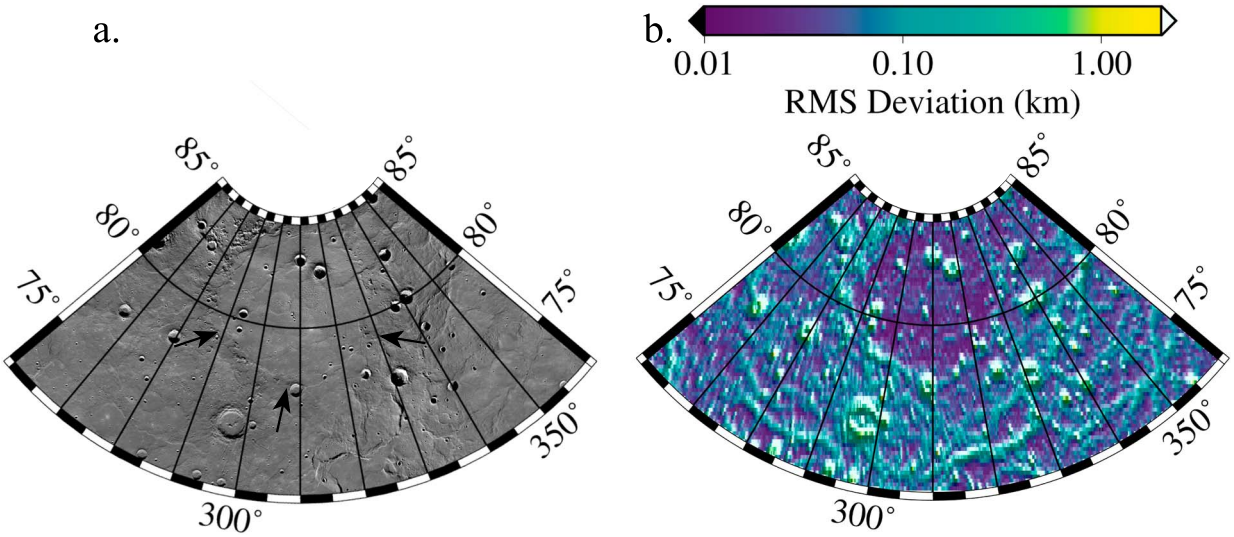

Figure 9. (a) The MDIS basemap (250 m/pixel, 750 nm) of the Goethe basin (box i in Figure 1) and the surrounding smooth plains. (b) The 5 km baseline surface roughness of the same region. In Figure 9b, Goethe basin has lower surface roughness values than the surrounding region. The higher density of tectonic shortening structures exterior to Goethe is visible in both the MDIS mosaic and the map of surface roughness; in the latter, the large ridge demarcating the buried basin rim is also visible (identified with black arrows). The map is in polar stereographic projection centered at 90°N.

At L = 5 km, many localized regions within the smooth plains show increased surface roughness values that are directly related to the presence of tectonic landforms (on the basis of their mapped distributions) [*Byrne et al*., 2014]. In Goethe basin, there is a clear reduction in the spatial density of shortening structures and an increase in the number of extensional structures (specifically graben and half graben) [*Watters et al*., 2012; *Klimczak et al*., 2012], which have smaller topographic expressions [*Byrne et al*., 2014] and are not readily resolved at the scale of our roughness maps. Of note, there is a large ridge demarcating the basin, into which the regional shortening strain has likely been partitioned and so reducing the spatial density of shortening structures within the basin itself. Although a decrease in impact crater areal density within Goethe would support the hypothesis that the basin's interior unit is younger than the surrounding smooth plains, studies of the crater density of the smooth plains as a whole have found no region in the smooth plains that is statistically younger than any other, and the eastern half of Goethe basin was found have a statistically higher crater density by *Ostrach et al*. [2015]. Finally, there is no spectral distinction or other type of geologic boundary between the plains within and exterior to the basin. We therefore conclude that the lower surface roughness in Goethe is a result of the relatively lower spatial density of shortening tectonic landforms within the basin, and not a function of the age of its interior smooth plains unit.

4.2.2. Northern Rise

The surface roughness measured at baselines investigated in this study shows that the 1000 km diameter northern rise (Figure 1b box ii) is indistinguishable from the surrounding smooth plains (Figure 10, although a slight hint of it appears at the 250 km baseline), which matches observations of MDIS images alone (where the rise is not visible and can only be resolved with topographic data). This finding confirms previous observations by *Zuber et al*. [2012], *Kreslavsky et al*. [2014], and *Fa et al*. [2016]. A deviogram of the northern rise (Figure 7) shows surface roughness values that are lower than the surface roughness of the entirety of the smooth plains, but this may be due to the lack of large complex craters that increase surface roughness. The formation of the northern rise likely did not modify roughness at scales of 0.5 to 250 km, and whatever process produced the northern rise occurred in such a manner as to not alter the surface topography for the baselines investigated—there is no surface deformation, e.g., faults, [*Byrne et al*., 2014] associated with the development of the rise. This in itself is not evidence for any specific formation mechanism but consists with the idea that the formation of the northern rise happened sufficiently slowly and/or deeply that brittle deformation of the upper crust did not occur. This inference is consistent with the relatively low surface strains accommodated from the northern rise [*Klimczak et al*., 2013].

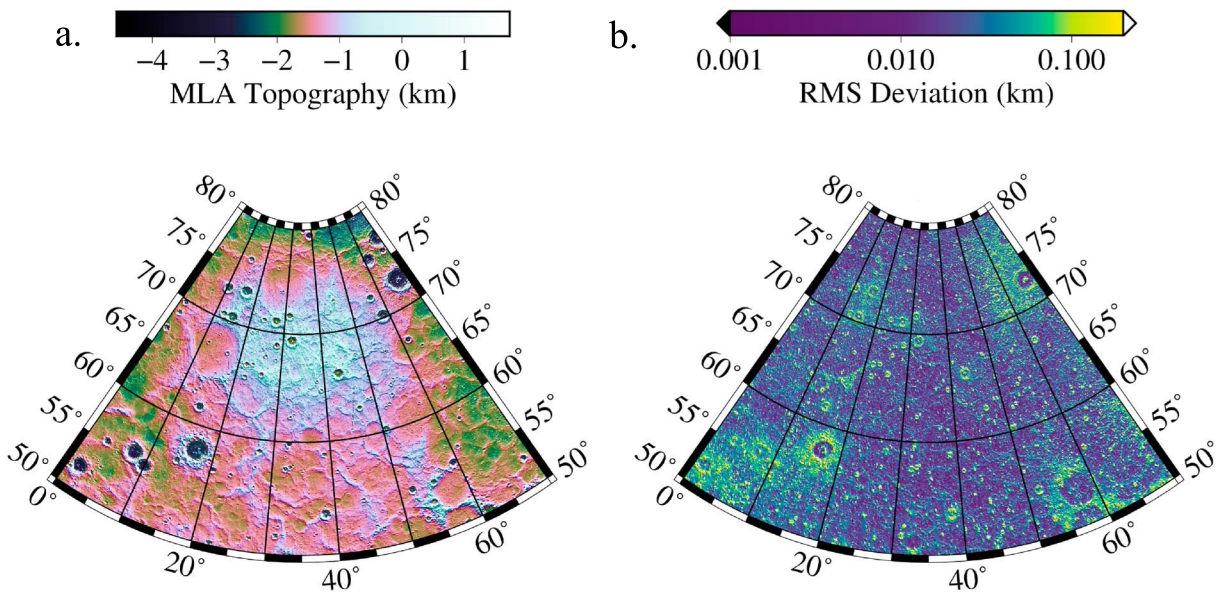

Figure 10. (a) The MLA topography of the northern rise (box ii in Figure 1). (b) The 1 km baseline surface roughness of the same region. As for other baselines, the northern rise is not distinguishable from the surrounding terrain. The formation of the northern rise did not result in any surface deformation resolvable with baselines from 500 m to 250 km. The map is in polar stereographic projection centered at 90°N.

4.3. Impact Craters

A relationship between impact crater areal density and surface roughness has been proposed for the Moon [*Rosenburg et al*., 2011, 2015] and for Mercury [*Fa et al*., 2016], arising from the bimodal distribution of surface roughness between the regions of lower crater density units (i.e., the lunar maria and Mercury's smooth plains) and higher crater density units (i.e., the lunar highlands and Mercury's cratered terrain). These studies showed that regions with higher spatial densities of impact craters have correspondingly higher surface roughness values, and regions with lower impact crater density have lower surface roughness values. We observe the same overall trend in this study; the value of surface roughness surrounding complex craters (i.e., their ejecta deposits and secondary fields) is greater compared to the smooth plains farther from the craters (Figure 1 box iii), similar to what was reported by *Fa et al*. [2016]. In particular, complex craters (those with diameters $>$50 km; Figure 11) and their expansive overlapping ejecta deposits and secondary crater fields may be a larger source of the differences in roughness between the smooth plains and the cratered terrain than that resulting from the spatial density of the craters themselves. This inference implies that a simple relationship might not exist between observed surface roughness and surface age on Mercury, as the ejecta and secondary craters of a complex crater affect the local surface roughness values to a greater extent than does the crater cavity itself. A deviogram of the surface roughness of the region encompassing the Gaudi and Stieglitz craters (Figure 7, the same craters shown in Figure 11), shows surface roughness values that are often higher than the surrounding smooth plains, particularly at baselines under 2 km.

4.4. Hurst Exponent and Comparison to Other Planetary Bodies

A Hurst exponent, H, was obtained from fits to deviograms (Figure 7) of the smooth plains and cratered terrains for $0.5 \leq L \leq 1.5$ km. At baselines larger than 1.5 km, no clear linear relationship (from which to derive a Hurst exponent) was found for either terrain between the log of the RMS deviation and the log of L. On Mercury, the Hurst exponent (at baselines of 0.5 to 1.5 km) may be a function of impact cratering or volcanism, since H is different between the smooth and cratered terrains. The maps of surface roughness show that tectonic deformation is also important but may be minor in comparison with volcanism and impact cratering.

It is not clear why the surface roughness of Mercury no longer displays a self-affine-like behavior above 1.5 km. The baseline L = 1.5 km is not correlated with the transition from simple to complex craters (which is found to occur at 11.8 km diameter for Mercury) [*Susorney et al*., 2016]. This lack of correlation of surface roughness values with the transition diameter from simple to complex craters was also found on the

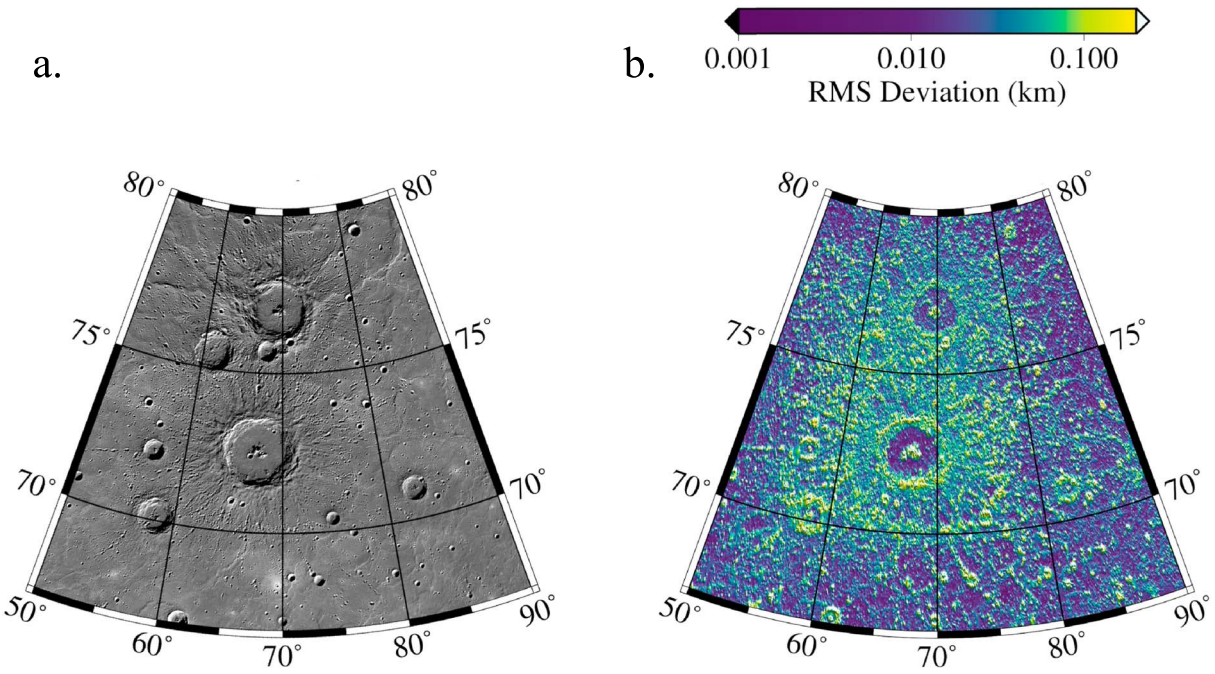

Figure 11. (a) The MDIS basemap (250 m/pixel, 750 nm) of the 81 km diameter Gaudi crater (top) and the 100 km diameter Stieglitz crater (bottom), both of which are surrounded by smooth plains (box iii in Figure 1). (b) The 1 km baseline surface roughness of the same region. The ejecta of Gaudi and Stieglitz dominate the surface at this baseline and generate similar roughness values to the cratered terrain [cf. *Whitten et al.*, 2014]. The map is in polar stereographic projection centered at 90°N.

Moon [*Rosenburg et al.*, 2011]. The break-over of the deviogram slope at 1.5 km for Mercury is more gradual than in studies of the Moon [e.g., *Rosenburg et al.*, 2011] or asteroid 433 Eros [e.g., *Cheng et al.*, 2002]; the deviograms on Mercury show a gradual change into a curved line that does not appear to level off in the larger baselines investigated. This finding is in contrast to deviograms for the Moon, which shows a clear break-over for the lunar highlands [*Rosenburg et al.*, 2011]. The gradual changes in the deviogram observed for Mercury may indicate a more complex interplay of processes influencing the topography of Mercury (e.g., higher density of secondary craters and tectonics) relative to that of the Moon.

Table 1 lists previously published values of the Hurst exponent for Mars, the Moon, 433 Eros, Earth, and Mercury at similar baselines to where a Hurst exponent could be fit on Mercury (in this study). With these data, we can compare the Hurst exponents of these five bodies for a similar range in baselines, and we focus here particularly on comparing the Moon and Mercury (the baseline range for the Moon is larger due to the closer spacing of laser altimeter footprints from the Lunar Reconnaissance Orbiter Lunar Orbiter Laser Altimeter instrument). Although Hurst exponents have been linked to specific geologic processes at smaller scales [e.g., *Morris et al.* [2008]], differences in Hurst exponents at the kilometer scale are not as well

Table 1. Comparisons of Hurst Exponents From Previous Studies

	Region	Hurst Exponent	Baseline Range (km)	Source
The Moon	Highlands	0.95 (median)	0.017–2.7	*Rosenburg et al.* [2011]
	Mare	0.76 (median)	0.017–2.7	*Rosenburg et al.* [2011]
Earth	Appalachian plateau	0.25–0.27	0.58–4.8	*Mark and Aronson* [1984]
	Basin and range	0.23–0.61	0.33–8.8	*Mark and Aronson* [1984]
	Ridge and valley	0.17–0.28	0.6–7.8	*Mark and Aronson* [1984]
433 Eros	Select tracks	0.81–0.91	0.003–0.20	*Cheng et al.* [2002]
Mars	Global	>0.5	0.3–3.0	*Orosei* [2003]
Mercury	Smooth plains	0.55–0.77	0.39–4.3	*Fa et al.* [2016]
	Intercrater plains	0.74–0.84	0.39–4.3	*Fa et al.* [2016]
	Heavily cratered terrain	0.76–0.86	0.39–4.3	*Fa et al.* [2016]
	Smooth plains	0.88 ± 0.01	0.5–1.5	This Study
	Cratered terrain	0.95 ± 0.01	0.5–1.5	This Study

understood. The Hurst exponents for the Moon (the closest analogue to Mercury in terms of observed surface processes though not surface gravity) have been explained by the higher density of craters in the lunar highlands (compared with the lunar mare) [*Rosenburg et al*., 2011]. The Hurst exponents for Mercury's cratered terrain and for the lunar highlands are in the same range with 0.95 ± 0.01 and 0.95, whereas the Hurst exponent of the smooth plains and lunar mare differs (0.88 ± 0.01 and 0.76, respectively). The difference in the Hurst exponent of the younger units on Mercury and the Moon may reflect a difference in the areal density of either impact craters (either primary or secondary) [*Ostrach et al*., 2015] or of tectonic landforms. Surface gravity differences between Mercury and the Moon may also be important, leading to more effective secondary cratering on Mercury. The similarity in the Hurst exponent between Mercury's cratered terrain and the lunar highlands is unexpected, since the lunar highlands have a higher spatial density of large primary complex craters compared with Mercury's cratered terrain [*Marchi et al*., 2013]. However, Mercury has a higher areal density of secondary craters as a result of the greater impactor velocity [e.g., *Strom et al*., 2008], which may counteract the reduction of primary craters on Mercury compared to the Moon, producing a terrain that is texturally similar to the lunar highlands.

Fa et al. [2016] measured the Hurst exponent at baselines of 0.39–4.3 km (due to their larger range in RMS deviation measurements and their selection of the L when the deviograms breaks-over) on Mercury and produced maps of the Hurst exponent. We did not produce similar maps here because of our requirement of having at least 100 measurements in each calculation of the Hurst exponent (following our stability assessment). Our values of the Hurst exponent for the smooth plains and cratered terrain differ from those of *Fa et al*. [2016], with their values being about 10% lower than ours. One possible source of this difference is our filtering of the data to accommodate both variable MLA track spacing and missing shot points, as well as our requirement for at least 100 points for each measurement of the Hurst exponent; the techniques used to select and filter data were not detailed in *Fa et al*. [2016]. Another possible source of the difference in Hurst exponent between this study and *Fa et al*. [2016] is the baselines chosen to measure the Hurst exponent. We calculated a Hurst exponent for approximately the baselines used by *Fa et al*. [2016], i.e., 0.5–4 km, and found Hurst exponents of 0.78 ± 0.02 and 0.81 ± 0.02 for the smooth plains and cratered terrains, respectively. This change in baselines the Hurst exponent is measure over is likely the main source of the discrepancy in Hurst exponents for our results and *Fa et al*. [2016], but we still report the values from L = 0.5–1.5 since we observe a turnover in the deviogram above L = 1.5 km.

5. Conclusion

The surface roughness (in terms of RMS deviation) of Mercury for two dominant morphological units in the planet's northern hemisphere was calculated for baselines between 0.5 km and 250 km for latitudes above 45°N. Maps were created to help investigate the role various geologic processes have had in modifying surface roughness. The main conclusions of this study include the following:

1. The surface roughness in our study region shows a bimodal distribution at all baselines. Regions of higher-surface roughness correspond to the more heavily cratered terrains, and regions of lower crater density have lower surface roughness values. This bimodal distribution corresponds to the two major geologic regions in Mercury's northern hemisphere, the smooth plains and cratered terrains, with the smooth plains having lower surface roughness values than the cratered terrains.
2. Impacts are the primary mechanism by which surface roughness values increase at baselines of 0.5 km to 250 km. A mixture of impact crater areal density and individual craters themselves (i.e., the morphology of the craters, including their rims, ejecta, and secondary crater fields) increases surface roughness.
3. Volcanism on Mercury has acted to reset the crater retention age and morphological texture of the planet's surface, which reduces the surface roughness values at all baselines investigated.
4. Variations of surface roughness within the smooth plains appear to be a function of the presence of both large complex craters (and their ejecta deposits) and tectonic landforms.
5. Such tectonic landforms include shortening structures, which are a minor but discernible contributor to surface roughness at small and medium baselines (0.5 km $< L <$ 20 km). The discernible character of such structures at $L <$ 20 km is reflected in low roughness values in Goethe basin, for example, where fewer shortening structures are observed within the basin relative to the higher spatial density of such landforms exterior to the basin, likely as a result of strain partitioning.

6. The ~1000 km diameter northern rise is not distinguishable from the surrounding smooth plains at baselines of 0.5 km to 250 km. This finding is consistent with previous studies of the rise, which found that its formation did not cause measurable deformation of the surface at these spatial scales.
7. The Hurst exponents for the smooth plains and the cratered terrain are 0.88 ± 0.01 and 0.95 ± 0.01, respectively, measured over baselines from 0.5 km to 1.5 km. The difference in the Hurst exponent between these two morphological units may reflect differences in crater areal density. The Hurst exponent for the cratered terrain is consistent with that measured Hurst exponent for the lunar highlands, whereas the Hurst exponent for the smooth plains is larger than the Hurst exponent for the lunar mare [*Rosenburg et al*., 2011]. The similar Hurst exponent for Mercury's cratered terrain and the lunar highlands implies that impact cratering may be the dominant geologic process since the Moon has fewer tectonic features than Mercury.

Acknowledgments
The MESSENGER project was supported by the NASA Discovery Program under contracts NASW-00002 to the Carnegie Institution of Washington and NAS5-97271 to The Johns Hopkins University Applied Physics Laboratory. Support was also provided by the Johns Hopkins University Applied Physics Laboratory Graduate Student Fellowship Program for H.C.M.S. and the Johns Hopkins University Applied Physics Laboratory Hafstad Fellowship program for O.S.B. MLA and MDIS data are freely available in the NASA Planetary Data System. Surface roughness data derived for this publication is available at https://zenodo.org/record/801574. We thank G.A. Neumann for assistance with MLA and comments on this paper. We thank Mikhail Kreslavsky, Jennifer Whitten, and Yasuhiro Yokota for their reviews and comments which improved the paper. Finally, we thank Steve Hauck and Wenzhe Fa for editorial handling.

References

Anderson, F. S., A. F. C. Haldemann, N. T. Bridges, M. P. Golombek, T. J. Parker, and G. Neumann (2003), Analysis of MOLA data for the Mars Exploration Rover landing sites, *J. Geophys. Res.*, *108*(E12), 8084, doi:10.1029/2003JE002125.

Barnouin-Jha, O. S., S. Baloga, and L. Glaze (2005), Comparing landslides to fluidized crater ejecta on Mars, *J. Geophys. Res.*, *110*, E04010, doi:10.1029/2003JE002214.

Barnouin-Jha, O. S., A. F. Cheng, T. Mukai, S. Abe, N. Hirata, R. Nakamura, R. W. Gaskell, J. Saito, and B. E. Clark (2008), Small-scale topography of 25143 Itokawa from the Hayabusa laser altimeter, *Icarus 198*, 108–124, doi:10.1016/j.icarus.2008.05.026.

Byrne, P. K., C. Klimczak, A. M. C. Şengör, S. C. Solomon, T. R. Watters, and S. A. Hauck II (2014), Mercury's global contraction much greater than earlier estimates, *Nat. Geosci.*, *7*, 301–307, doi:10.1038/ngeo2097.

Byrne, P. K., L. R. Ostrach, C. I. Fassett, C. R. Chapman, B. W. Denevi, A. J. Evans, C. Klimczak, M. E. Banks, J. W. Head, and S. C. Solomon (2016), Widespread effusive volcanism on Mercury likely ended by about 3.5 Ga, *Geophys. Res. Lett. 43*, 7408–7416, doi:10.1002/2016GL069412.

Chabot, N. L., C. M. Ernst, J. K. Harmon, S. L. Murchie, S. C. Solomon, D. T. Blewett, and B. W. Denevi (2013), Craters hosting radar-bright deposits in Mercury's north polar region: Areas of persistent shadow determined from MESSENGER images, *J. Geophys. Res. Planets*, *118*, 26–36, doi:10.1029/2012JE004172.

Cheng, A. F., O. Barnouin-Jha, L. Prockter, M. T. Zuber, G. Neumann, D. E. Smith, J. Garvin, M. Robinson, J. Veverka, and P. Thomas (2002), Small-scale topography of 433 Eros from laser altimetry and imaging, *Icarus*, *155*, 51–74, doi:10.1006/icar.2001.6750.

Denevi, B. W., M. S. Robinson, S. C. Solomon, S. L. Murchie, D. T. Blewett, D. L. Domingue, T. J. McCoy, C. M. Ernst, J. W. Head, and T. R. Watters (2009), The evolution of Mercury's crust: A global perspective from MESSENGER, *Science*, *324*, 613–618, doi:10.1126/science.1172226.

Denevi, B. W., et al. (2013), The distribution and origin of smooth plains on Mercury, *J. Geophys. Res. Planets*, *118*, 891–907, doi:10.1002/jgre.20075.

Fa, W., Y. Cai, Z. Xiao, and W. Tian (2016), Topographic roughness of the northern high latitudes of Mercury from MESSENGER Laser Altimeter data, *Geophys. Res. Lett.*, *43*, 3078–3087, doi:10.1002/2016GL068120.

Gault, D. E., J. E. Guest, J. B. Murray, D. Dzurisin, and M. C. Malin (1975), Some comparisons of impact craters on Mercury and the Moon, *J. Geophys. Res.*, *80*, 2444–2460, doi:10.1029/JB080i017p02444.

Glaze, L. S., S. M. Baloga, and E. R. Stofan (2003), A methodology for constraining lava flow rheologies with MOLA, *Icarus*, *165*, 26–33, doi:10.1016/S0019-1035(03)00171-4.

Harmon, J. K. (1997), Mercury radar studies and lunar comparisons, *Adv. Space Res.*, *19*(10), 1487–1496, doi:10.1016/S0273-1177(97)00347-5.

Harmon, J. K. (2007), Radar imaging of Mercury, *Space Sci. Rev.*, *132*, 307–349, doi:10.1007/s11214-007-9234-y.

Harmon, J. K., P. J. Perillat, and M. A. Slade (2001), High-resolution radar imaging of Mercury's north pole, *Icarus*, *149*, 1–15, doi:10.1006/icar.2000.6544.

Harmon, J. K., M. A. Slade, B. J. Butler, J. W. I. Head, M. S. Rice, and D. B. Campbell (2007), Mercury: Radar images of the equatorial and mid-latitude zones, *Icarus*, *187*, 374–405, doi:10.1016/j.icarus.2006.09.026.

Head, J. W., et al. (2008), Volcanism on Mercury: Evidence from the first MESSENGER flyby, *Science*, *321*, 69–72, doi:10.1126/science.1159256.

Head, J. W., et al. (2011), Flood volcanism in the northern high latitudes of Mercury revealed by MESSENGER, *Science*, *333*, 1853–1856, doi:10.1126/science.1211997.

Klimczak, C., T. R. Watters, C. M. Ernst, A. M. Freed, P. K. Byrne, S. C. Solomon, D. M. Blair, and J. W. Head (2012), Deformation associated with ghost craters and basins in volcanic smooth plains on Mercury: Strain analysis and implications for plains evolution, *J. Geophys. Res.*, *117*, E00L03, doi:10.1029/2012JE004100.

Klimczak, C., C. M. Ernst, P. K. Byrne, S. C. Solomon, T. R. Watters, S. L. Murchie, F. Preusker, and J. A. Balcerski (2013), Insights into the subsurface structure of the Caloris basin, Mercury, from assessments of mechanical layering and changes in long-wavelength topography, *J. Geophys. Res. Planets*, *118*, 2030–2044, doi:10.1002/jgre.20157.

Kreslavsky, M. A., and J. W. Head (2000), Kilometer-scale roughness of Mars: Results from MOLA data analysis, *J. Geophys. Res.*, *105*, 26,695–26,711, doi:10.1029/2000JE001259.

Kreslavsky, M. A., J. W. Head, and J. K. Harmon (2008), Large-scale topographic roughness of terrestrial planets: A comparison, *Lunar Planet. Sci.*, *39*, abstr. 1472.

Kreslavsky, M. A., J. W. Head, G. A. Neumann, M. A. Rosenburg, O. Aharonson, D. E. Smith, and M. T. Zuber (2013), Lunar topographic roughness maps from Lunar Orbiter Laser Altimeter (LOLA) data: Scale dependence and correlation with geologic features and units, *Icarus*, *226*, 52–66, doi:10.1016/j.icarus.2013.04.027.

Kreslavsky, M. A., J. W. Head, and G. A. Neumann (2014), Kilometer-scale topographic roughness of Mercury: Correlation with geologic features and units, *Geophys. Res. Lett.*, *41*, 8245–8251, doi:10.1002/2014GL062162.

Kucinskas, A. B., D. L. Turcotte, J. Huang, and P. G. Ford (1992), Fractal analysis of Venus topography in Tinatin Planitia and Ovda Regio, *J. Geophys. Res.*, *97*, 13,635–13,641, doi:10.1029/92JE01132.

Marchi, S., C. R. Chapman, C. I. Fassett, J. W. Head, W. F. Bottke, and R. G. Strom (2013), Global resurfacing of Mercury 4.0–4.1 billion years ago by heavy bombardment and volcanism, *Nature*, *499*, 59–61, doi:10.1038/nature12280.

Mark, D. M., and P. B. Aronson (1984), Scale-dependent fractal dimensions of topographic surfaces: An empirical investigation, with applications in geomorphology and computer mapping, *Math. Geol.*, *16*, 671–683, doi:10.1007/BF01033029.
Morris, A. R., F. S. Anderson, P. J. Mouginis-Mark, A. F. C. Haldemann, B. A. Brooks, and J. Foster (2008), Roughness of Hawaiian volcanic terrains, *J. Geophys. Res.*, *113*, E12007, doi:10.1029/2008JE003079.
Orosei, R. (2003), Self-affine behavior of Martian topography at kilometer scale from Mars Orbiter Laser Altimeter data, *J. Geophys. Res.*, *108*(E4), 8023, doi:10.1029/2002JE001883.
Ostrach, L. R., M. S. Robinson, J. L. Whitten, C. I. Fassett, R. G. Strom, J. W. Head, and S. C. Solomon (2015), Extent, age, and resurfacing history of the northern smooth plains on Mercury from MESSENGER observations, *Icarus*, *250*, 602–622, doi:10.1016/j.icarus.2014.11.010.
Perron, J. T., J. W. Kirchner, and W. E. Dietrich (2008), Spectral signatures of characteristic spatial scales and nonfractal structure in landscapes, *J. Geophys. Res.*, *113*, F04003, doi:10.1029/2007JF000866.
Pike, R. J. (1988), Geomorphology of impact craters on Mercury, in *Mercury*, edited by F. Vilas, C. R. Chapman, and M. S. Matthews, pp. 165–273, Univ. of Arizona Press, Tucson, Ariz.
Pommerol, A., S. Chakraborty, and N. Thomas (2012), Comparative study of the surface roughness of the Moon, Mars and Mercury, *Planet. Space Sci.*, *73*, 287–293, doi:10.1016/j.pss.2012.08.020.
Robbins, S. J., and B. M. Hynek (2013), Utility of laser altimeter and stereoscopic terrain models: Application to Martian craters, *Planet. Space Sci.*, *86*, 57–65, doi:10.1016/j.pss.2013.06.019.
Rosenburg, M. A., O. Aharonson, J. W. Head, M. A. Kreslavsky, E. Mazarico, G. A. Neumann, D. E. Smith, M. H. Torrence, and M. T. Zuber (2011), Global surface slopes and roughness of the Moon from the Lunar Orbiter Laser Altimeter, *J. Geophys. Res.*, *116*, E02001, doi:10.1029/2010JE003716.
Rosenburg, M. A., O. Aharonson, and R. Sari (2015), Topographic power spectra of cratered terrains: Theory and application to the Moon, *J. Geophys. Res. Planets*, *120*, 177–194, doi:10.1002/2014JE004746.
Schultz, P. H. (1988), Cratering on Mercury: A relook, in *Mercury*, edited by F. Vilas, C. R. Chapman, and M. S. Matthews, pp. 165–273, Univ. of Arizona Press, Tucson, Ariz.
Shepard, M. K., and B. A. Campbell (1999), Radar scattering from a self-affine fractal surface: Near-nadir regime, *Icarus*, *141*, 156–171, doi:10.1006/icar.1999.6141.
Shepard, M. K., B. A. Campbell, M. H. Bulmer, T. G. Farr, L. R. Gaddis, and J. J. Plaut (2001), The roughness of natural terrain: A planetary and remote sensing perspective, *J. Geophys. Res.*, *106*, 32,777–32,796, doi:10.1029/2000JE001429.
Smith, W. H. F., and P. Wessel (1990), Gridding with continuous curvature splines in tension, *Geophysics*, *55*, 293–305, doi:10.1190/1.1442837.
Spudis, P. D., and J. E. Guest (1988), Stratigraphy and geologic history of Mercury, in *Mercury*, edited by F. Vilas, C. R. Chapman, and M. S. Matthews, pp. 165–273, Univ. of Arizona Press, Tucson, Ariz.
Strom, R. G. (1979), Mercury: A post-Mariner 10 assessment, *Space Sci. Rev.*, *24*, 3–70, doi:10.1007/BF00221842.
Strom, R. G., C. R. Chapman, W. J. Merline, S. C. Solomon, and J. W. Head (2008), Mercury cratering record viewed from MESSENGER's first flyby, *Science*, *321*, 79–81, doi:10.1126/science.1159317.
Strom, R. G., N. J. Trask, and J. E. Guest (1975), Tectonism and volcanism on Mercury, *J. Geophys. Res.*, *80*, 2478–2507, doi:10.1029/JB080i017p02478.
Susorney, H. C. M., O. S. Barnouin, C. M. Ernst, and C. L. Johnson (2016), Morphometry of impact craters on Mercury from MESSENGER altimetry and imaging, *Icarus*, *271*, 180–193, doi:10.1016/j.icarus.2016.01.022.
Talpe, M. J., M. T. Zuber, D. Yang, G. A. Neumann, S. C. Solomon, E. Mazarico, and F. Vilas (2012), Characterization of the morphometry of impact craters hosting polar deposits in Mercury's north polar region, *J. Geophys. Res.*, *117*, E00L13, doi:10.1029/2012JE004155.
Trask, N. J., and J. E. Guest (1975), Preliminary geologic terrain map of Mercury, *J. Geophys. Res.*, *80*, 2461–2477, doi:10.1029/JB080i017p02461.
Turcotte, D. L. (1997), *Fractals and Chaos in Geology and Geophysics*, 2nd ed., 398 pp., Cambridge Univ. Press, New York.
Watters, T. R., S. C. Solomon, M. S. Robinson, J. W. Head, S. L. Andre, S. A. I. Hauck, and S. L. Murchie (2009), The tectonics of Mercury: The view after MESSENGER'S first flyby, *Earth Planet. Sci. Lett.*, *285*, 283–296, doi:10.1016/j.epsl.2009.01.025.
Watters, T. R., S. C. Solomon, C. Klimczak, A. M. Freed, J. W. Head, C. M. Ernst, D. M. Blair, T. A. Goudge, and P. K. Byrne (2012), Extension and contraction within volcanically buried impact craters and basins on Mercury, *Geology*, *40*, 1123–1126, doi:10.1130/G33725.1.
Wessel, P., W. H. F. Smith, R. Scharroo, J. Luis, and F. Wobbe (2013), Generic Mapping Tools: Improved version released, *Eos*, *94*, 409–410, doi:10.1002/2013EO450001.
Whitten, J. L., J. W. Head, B. W. Denevi, and S. C. Solomon (2014), Intercrater plains on Mercury: Insights into unit definition, characterization, and origin from MESSENGER datasets, *Icarus*, *241*, 97–113, doi:10.1016/j.icarus.2014.06.013.
Yang, D., M. T. Zuber, J. W. Head, and S. C. Solomon (2013), Distribution of topographic slope and roughness in Mercury's northern hemisphere, *Lunar Planet. Sci.*, *44*, abstr. 2347.
Yokota, Y., et al. (2014), Variation of the lunar highland surface roughness at baseline 0.15–100 km and the relationship to relative age, *Geophys. Res. Lett.*, *41*, 1444–1451, doi:10.1002/2013GL059091.
Zuber, M. T., et al. (2012), Topography of the northern hemisphere of Mercury from MESSENGER Laser Altimetry, *Science*, *336*, 217–220, doi:10.1126/science.1218805.